Supporting Information

Neisius et al. 10.1073/pnas.1319203111

SI Materials and Methods

Lens Design and Fabrication. The annular ring modification of the lens design delays the propagation of the outer portion of an incident plane wave generated by the EM coil by a time step

$$\Delta t = h \cdot \left(\frac{1}{c_0} - \frac{1}{c_l} \right), \qquad \textbf{[S1]}$$

where c_l (2.40 km/s) and c_0 (1.49 km/s) are the longitudinal (or P) wave speeds in the lens and water, respectively. The inner portion of the incident plane wave is refracted through the central, uncut region of the lens, forming the new leading lithotripter shock wave (LSW). Because of the reduced source aperture, the focal width (FW) of the leading LSW is broadened while superposition of the time-delayed wave with the leading LSW alters the pulse profile (1). The inner radius of the annulus (R_u = 56.2 mm) determines the area ratio of uncut to total lens surface, that is,

$$AR = \frac{R_u^2 - R_i^2}{R_o^2 - R_i^2}, \qquad \textbf{[S2]}$$

where R_i (16.9 mm) and R_o (68.6 mm) are radii of the lens aligned to the inner and outer edges of the coil within the source, respectively (Fig. 1*C*).

The acoustic focusing distances produced by spherical and ellipsoidal lens surface modifications were estimated using a multiphysics computational model of wave propagation. The model employs a finite-volume conservation law Riemann solver (2) within the BEARCLAW framework developed by S.M. and solves the linear elasticity and Euler equations simultaneously to simulate wave propagation within the focusing lens and water domains, respectively. Input plane wave pressure for the numerical model was measured using a fiber optic probe hydrophone (FOPH) and curve-fitted as described previously (3). As a derivation of FOPH measurements, uncertainty in numerical model results is 5% at minimum (4).

The 3D shape of the acoustic lens was designed using Autodesk Inventor CAD software and then exported to MasterCam (CNC Software), where the material removal machining motions were programmed. Using a Centroid CNC lathe and carbide turning tools, the excess material was removed in 2-mm steps to form the shape of the new lens. After machining, all surfaces of the lens were polished using an ultrafine aluminum silicate polishing pad (Scotch Brite 9767; 3M).

In Vitro Characterization of Lenses. Acoustic fields produced by the original and new lenses were characterized using the FOPH, which was fastened to a 3D positioning stage controlled remotely using a program written in MATLAB (MathWorks). The axisymmetric electromagnetic (EM) shock source with either the original or new lens was mounted at the base of a Lucite tank (length × width × height, 43 × 39 × 29 cm) filled with 0.2-μm-filtered and degassed water (<3 mg/L O_2 concentration, ~21 °C). Pressure waveforms were measured in four quadrants in the lithotripter focal plane using radial step sizes of 1 mm ($0 < r < 6$ mm) and 2 mm ($6 < r < 14$ mm). Along the lithotripter (z) axis, pressure waveforms were measured in 5-mm intervals (-20 mm $< z < +20$ mm) and 10-mm intervals (-60 mm $< z < -20$ mm and $+20$ mm $< z < +60$ mm). FOPH waveforms were recorded at 100-MHz sampling frequency using a LeCroy Waverunner 6050a digital oscilloscope (Teledyne LeCroy) and transferred for off-line calibration and postprocessing using MATLAB. *FW* was calculated as the full width at half maximum peak pressure (p_+), and the derived total acoustic pulse energy was determined by

$$E_{tot} = \frac{2\pi}{Z_0} \cdot \int_0^{R_c} \int_{t_1}^{t_2} p_a(r,t)^2 \cdot r dt dr, \qquad \textbf{[S3]}$$

where Z_0 (1.5 MRayls) is the acoustic impedance of water, R_c (6 mm) is a radius encompassing most stones treated with shock wave lithotripsy (SWL), $p_a(r,\tau)$ is acoustic pressure from the LSW, and time values (t_1 and t_2) are the first and final crossing points of 10% of the local p_+ by the $p_a(r,t)$. Eq. **S3** is also used to calculate compressive and secondary acoustic pulse energies, with t_1 and t_2 defined as the first and final crossing points of 10% of the local p_+ by the applicable wave section.

In Vitro Stone Comminution. In membrane holder experiments, a 20-gauge syringe needle sandwiched between the edge of two membranes (Fig. S2*A*) was used to allow for pressure release inside the membrane holder, which reduces fluid and fragment mixing effects during SWL (5). In simulated respiratory motion experiments, the 3D positioning system was used to translate the flat-base tube holder along a single horizontal axis within the lithotripter focal plane during SWL. Four different phases of respiration (i.e., inspiration, inspiration pause, expiration, and expiration pause) were simulated following typical kidney motion patterns observed in patients (6). The holder was translated in the inferior direction (away from the lithotripter focus) during inspiration and returned in the superior direction to the focal region during expiration (Fig. 4*C*). The simulated breath rate (12 breaths per minute) and excursion distances (D = 5 or 15 mm) were representative of kidney displacement in patients during SWL under heavy or light sedation, respectively (7). Randomization factors were incorporated to avoid discrete translation patterns. Histograms of the motion patterns used during comminution tests were statistically similar between the two lenses (Fig. 4*C*).

In Vivo Stone Comminution. Female farm pigs with an approximate weight of 50 kg were used as animal models because their kidney size and anatomy are similar to those of human kidneys (8). Eleven pigs were used to compare fragmentation efficiency produced by the Siemens Modularis EM lithotripter using either the original or new lens. Animals were placed under general endotracheal anesthesia and shaved along their flanks to improve coupling quality across the skin surface. Subsequently, animals were transferred to an operation table for midline laparotomy. After bowel mobilization, the retroperitoneal space was opened to expose the proximal ureter close to the renal pelvis. A proximal ureterotomy of ~1 cm was performed, and a cylindrical BegoStone phantom was inserted and guided into the renal pelvis (Fig. 5*A*). Through the existing ureterotomy, a 6-french polyurethane double-J ureteral stent (Boston Scientific) was advanced into the renal pelvis to prevent stone and fragment migration to the ureter during and after SWL. The ureterotomy was closed with a 4/0 running monofilament suture. This procedure was repeated on the opposite kidney. After closing the laparotomy, the animal was transferred to the lithotripsy table.

Before SWL, ultrasound gel (Medline) was applied on the coupling bellow of the shock head, and the lithotripter focus was aligned to an implanted stone under fluoroscopic guidance (Fig. 5*B*). The bellow was then carefully inflated to establish skin contact to minimize air pockets trapped at the coupling interface. Afterward, a constant bellow pressure was maintained (9) during the entire therapy session in which 3,000 shocks were delivered to each kidney at a pulse repetition frequency of 1.5 Hz. In the first 800 shocks, a ramping scheme of incrementally increasing acoustic pulse energy was used, which has been successfully used in clinics for patient treatment (10, 11). After the initial 500 shocks, the treatment was paused for 4 min before resuming at higher output levels, which has been suggested as a protective measure against SWL-induced tissue injury in animal models (12). From 800 to 3,000 shocks, the maximum source voltage (i.e., 14.8 kV for the original lens or 18.1 kV for the new lens) was applied, resulting in ∼112 J of cumulative acoustic pulse energy (E_+) delivered to the focal region. Stone movement and spreading were checked with fluoroscopy in situ after 200, 500, 800, and 1,000 shocks. To avoid potential operator bias to the comminution results, no realignment of lithotripter focus was performed after 500 shocks, even when fragments spread to different (upper or lower) calyces after the initial fracture. Post-SWL, the pigs were killed. Ureters were ligated to avoid any loss of fragments, and the kidneys were harvested and bivalved. Each sample was photographed, and fragments were collected for analysis. In comparisons of in vivo comminution rates, a subgroup analysis was performed to consider experimental biases from either incidental confinement of stones by double-J stent loop during the entire treatment (i.e., stones that were prevented from spreading naturally) or abnormal fragment spread (i.e., large fragment migration to an off-focus calyx).

Tissue Injury Assessment. Following general anesthesia of the animal, a cystoscopy was performed to place an open-ended 6-french ureteral catheter (Cook Medical) in a retrograde fashion into the kidney collecting system. To align the lithotripter focus to the lower part of the middle calyx of each kidney, fluoroscopic agent Isoview-300 (Bracco Diagnostics) was injected through the catheter. After complete drainage of the contrast medium, SWL was performed. Post-SWL, the skin surface at the LSW entrance site was photographed. Following killing and kidney excision, additional photographs were taken from the anterior and posterior sides of the kidneys, as well as surrounding organs/tissues to document any visible gross injury.

For microscopic tissue injury assessment, fully fixed kidneys were serially sliced in the coronal plane at 3-mm intervals. Both surfaces of each slice were photographed. Slices that included the SWL target site as well as other areas showing evidence of injury were divided into 2- × 2-cm blocks for histologic processing using a numbered grid to facilitate reassembly of stained section images into a virtual organ of whole mount slices. These blocks were processed and paraffin-embedded, and 5-μm-thick sections were stained with hematoxylin and eosin. All resulting sections were imaged at high resolution (2,400 pixels per inch) using a digital flat-bed scanner (PIXMA MP470; Canon), and the resulting images were assembled into virtual whole mount images using Photoshop CS3 (Adobe Systems) supplemented by Fovea Pro-4.0 (Reindeer Graphics).

1. Zhong P, Smith N, Simmons NW, Sankin G (2011) A new acoustic lens design for electromagnetic shock wave lithotripters. *10th International Symposium on Therapeutic Ultrasound* (*Istu 2010*), (American Institute of Physics, Melville, NY), Vol 1359, pp 42–47.
2. LeVeque RJ (1997) Wave propagation algorithms for multidimensional hyperbolic systems. *J Comput Phys* 131(2):327–353.
3. Smith N, et al. (2012) A comparison of light spot hydrophone and fiber optic probe hydrophone for lithotripter field characterization. *Rev Sci Instrum* 83(1):014301.
4. Fovargue DE, et al. (2013) Experimentally validated multiphysics computational model of focusing and shock wave formation in an electromagnetic lithotripter. *J Acoust Soc Am* 134(2):1598–1609.
5. Qin J, Simmons WN, Sankin G, Zhong P (2010) Effect of lithotripter focal width on stone comminution in shock wave lithotripsy. *J Acoust Soc Am* 127(4):2635–2645.
6. Davies SC, Hill AL, Holmes RB, Halliwell M, Jackson PC (1994) Ultrasound quantitation of respiratory organ motion in the upper abdomen. *Br J Radiol* 67(803):1096–1102.
7. Bromage PR, Bonsu AK, el-Faqih SR, Husain I (1989) Influence of Dornier HM3 system on respiration during extracorporeal shock-wave lithotripsy. *Anesth Analg* 68(3):363–367.
8. Connors BA, et al. (2012) Evaluation of shock wave lithotripsy injury in the pig using a narrow focal zone lithotriptor. *BJU Int* 110(9):1376–1385.
9. Neucks JS, et al. (2008) Improved acoustic coupling for shock wave lithotripsy. *Urol Res* 36(1):61–66.
10. Zhou YF, Cocks FH, Preminger GM, Zhong P (2004) The effect of treatment strategy on stone comminution efficiency in shock wave lithotripsy. *J Urol* 172(1):349–354.
11. Maloney ME, et al. (2006) Progressive increase of lithotripter output produces better in-vivo stone comminution. *J Endourol* 20(9):603–606.
12. Connors BA, et al. (2009) Effect of initial shock wave voltage on shock wave lithotripsy-induced lesion size during step-wise voltage ramping. *BJU Int* 103(1):104–107.

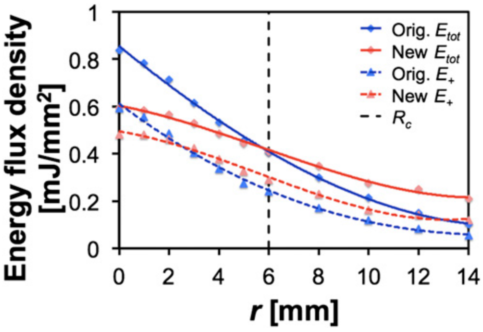

Fig. S1. Energy flux density. A comparison of energy flux densities curve-fitted with trinomials, which are used in the calculation of total acoustic pulse energy (E_{tot}) and compressive acoustic pulse energy (E_+) for the original and new lenses. R_c is the radius for pulse energy calculation and represents a threshold that encompasses most stones treated with SWL.

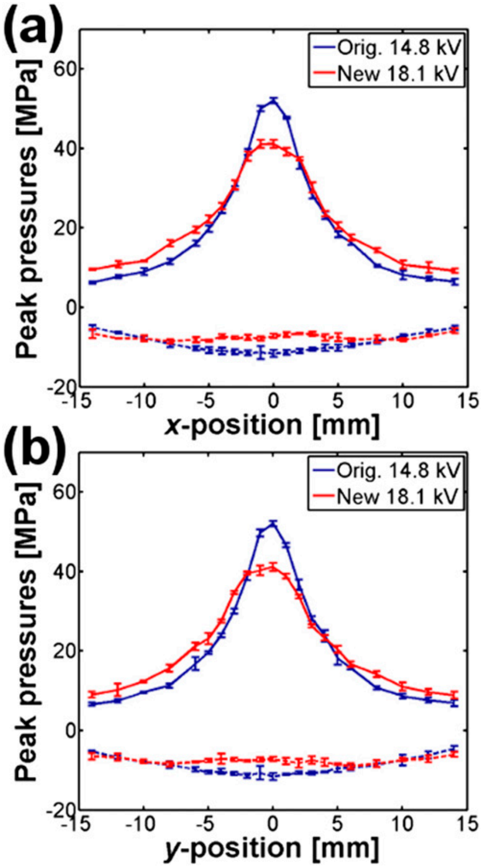

Fig. S2. Lens characterization. Averaged peak positive (p_+) and negative (p_-) pressures at $z = 0$ mm measured along the (*A*) *x* and (*B*) *y* axes of the symmetric EM source.

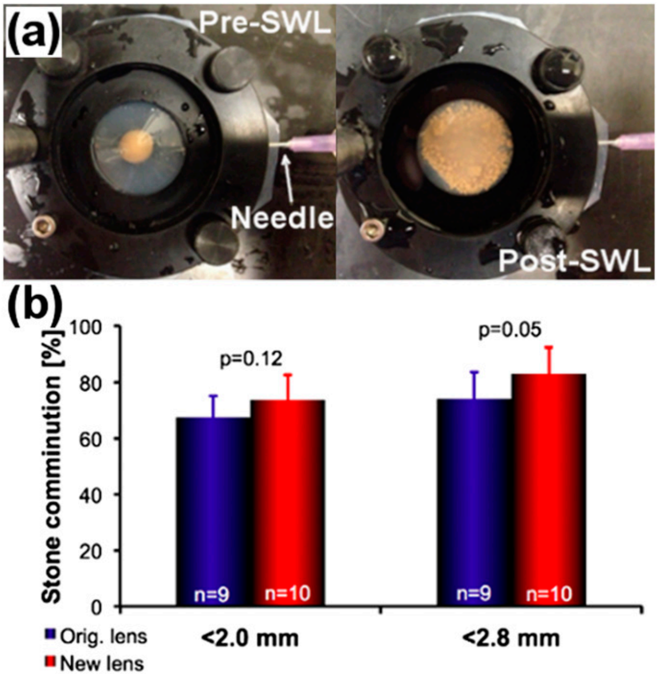

Fig. S3. In vitro stone comminution. (*A*) Representative (*Left*) pre- and (*Right*) post-SWL images of stone comminution in the membrane holder positioned at the lithotripter focus. (*B*) Stone comminution results in the membrane holder using two mesh sizes for fragment collection.